Facet-dependent Oxygen Evolution Reaction Activity of IrO_2 from Quantum Mechanics and Experiments

Soonho Kwon,[1]† Kelsey A. Stoerzinger,[2]† Reshma Rao,[3] Liang Qiao,[4] William A. Goddard III,[1]* Yang Shao-Horn[5,6,7]*

[1]Materials and Process Simulation Center (MSC), California Institute of Technology, Pasadena, CA 91125, USA

[2]Department of Chemical Engineering and Materials Science, University of Minnesota, Minneapolis, MN 55455, USA

[3]Department of Materials, Imperial College London, South Kensington Campus, London SW7 2AZ, U.K.

[4]Center for Nanophase Materials Sciences, Oak Ridge National Laboratory, 1 Bethel Valley Road, Oak Ridge, Tennessee 37831, United States

[5]Department of Materials Science and Engineering, Massachusetts Institute of Technology, Cambridge, MA 02139, USA

[6]Research Laboratory of Electronics, Massachusetts Institute of Technology, Cambridge, MA 02139, USA

[7]Department of Mechanical Engineering, Massachusetts Institute of Technology, Cambridge, MA 02139, USA

†These authors contributed equally to this work.

*Corresponding authors: wag:wag@caltech.edu; shaohorn@mit.edu

ORCID: SK: 0000-0002-9225-3018

ORCID: KAS: 0000-0002-3431-8290

ORCID: RR: 0000-0002-6655-3105

ORCID: LQ: 0000-0003-2400-2986

ORCID: WAG:0000-0003-0097-5716

ORCID: YSH: 0000-0001-8714-2121

One Sentence Summary:

We predicted the facet-dependent Oxygen Evolution Reaction (OER) activity of IrO_2 from Quantum Mechanics in agreement with new experimental data on five facets, elucidating facet-dependent mechanisms and atomistic understanding of unique rate limiting steps.

Abstract

The diversity of chemical environments present on unique crystallographic facets can drive dramatic differences in catalytic activity and reaction mechanism. By coupling experimental investigations of five different IrO_2 facets and theory, we characterize the detailed elemental steps of the surface redox processes and the rate-limiting processes for the oxygen evolution reaction (OER). The predicted complex evolution of surface adsorbates and the associated charge transfer as a function of applied potential matches well the distinct redox features observed experimentally for the five facets. Our microkinetic model from with Grand Canonical Quantum Mechanics (GC-QM) calculations demonstrates mechanistic differences between nucleophilic attack and O-O coupling across facets, providing the rates as a function of applied potential. These GC-QM calculations explain the higher OER activity observed on (100), (001), and (110) facets and the lower activity observed for (101) and (111) facets. This combined study with theory and experiment brings new insights into the structural features that either promote or hinder the OER activity of IrO_2, which are expected to provide parallels in structural effects on other oxide surfaces.

Key words: OER, IrO_2 Thin film, Pulsed laser deposition, DFT, Reaction mechanism, Microkinetics

Introduction

IrO_2 is highly active and stable for the oxygen evolution reaction (OER) and the electrocatalyst of choice for proton exchange membrane (PEM) electrolyzers.[1] Given the scale of green hydrogen deployment, even subtle gains in IrO_2 activity or stability can substantially decrease loading and reduce system cost. Under reaction conditions, Ir is oxidized, and most stable when synthesized in the rutile crystal structure[2] rather than the amorphous phases formed by thermal or electrochemical oxidation.[3] The rutile crystal structure can be terminated with a number of different crystallographic facets that differ in their propensity for surface oxidation and distance between Ir sites—expected to influence interaction between reaction intermediates. Given that the performance of IrO_2 electrolyzers is limited by OER kinetics at the anode,[4] understanding the orientation-dependence of these kinetics would enable efficiency gains by modifying crystallographic texture. Furthermore, mechanistic understanding can suggest strategies for catalyst design that directly translate to improved OER kinetics.The stoichiometric surface of rutile IrO_2 exposes coordinatively unsaturated (CUS) sites, which have been considered to be the active sites for water oxidation[5], analogous to that of rutile RuO_2.[6] With increasing potential, IrO_2 reacts with water and desorbs protons and other adsorbates upon (electro)chemical oxidation. The progression between adsorbed species is coupled with charge transfer to/from the surface,[7] resulting in the "redox" features observed in cyclic voltammetry. The potential at which these features occur is related to the stability of corresponding adsorbates, and the total charge passed is related to their concentration on the surface.[8] Thus, understanding differences in these features across facets can illuminate the tendencies of electrochemical oxidation that should prove useful in controlling catalytic activity of OER.[9]

OER activity depends on the reaction mechanism and the energetics between successive intermediate species.[10,11] The rate-determining step of OER on IrO_2 has been proposed to be O-O bond formation, which can be formed by water nucleophilic attack ($*O + H_2O \rightarrow *OOH + H^+ + e^-$) or by direct oxo coupling ($*O + *O \rightarrow *O\text{-}*O$)[7]. The dominant mechanisms depend on the adsorbate binding energy, their surface population at a given applied potential,[12] and on the distance between reactive species—all of which depend on the crystallographic facet.[13,14] For rutile RuO_2, OER activity varies amongst crystallographic orientation,[15] and calculations indicate the local environment of the CUS sites gives rise to differences in adsorbate binding strength[16] and

subsequent changes in the rate determining step.[6,14] Missing, however, is a direct comparison between the voltammetric response and theory incorporating the applied potential and equilibrium surface coverage for different facets of oxides such as rutile IrO_2.

In this study, we make a direct comparison of cyclic voltammetry between theory and experiment for five rutile IrO_2 facets. In contrast to typical attribution of redox features as a specific redox couple, our calculations reveal complex changes in surface chemistry including substantial contributions from changes at the bridging oxygen sites (μ_2-O) and partial contribution of multiple redox couples to a single redox peak. In our experiment in acid, the OER activity is the highest for (100), followed by (001) and (110), whereas (101) and (111) are much less active. To find the origin of this activity trend, we performed microkinetic analysis with the energetics from the Grand Canonical Potential Kinetics (GCP-K) [17,18] allowing atomic-scale interpretation of physical processes with explicit consideration of the applied potential—a factor commonly overlooked but crucial in describing electrochemistry.[19,20]

We find that the mechanism of O-O coupling and the rate limiting step are facet- and potential-dependent, as are the identity of sites involved in this step. Our findings are further supported by the excellent agreement observed between our experimental results and the unified theoretical framework, which includes geometric, electronic, chemical kinetic, and applied bias effects. This alignment lends significant credibility to our study and offers an atomistic comprehension of the facet-dependent voltammetric current response of IrO_2.

Results & Discussion.

Rutile films with (100), (110), (001), (101), and (111) orientations were grown by pulsed laser deposition (PLD) under conditions reported previously[15] and detailed in the Experimental Methods. The orientation was confirmed by X-ray diffraction (**Fig. S1A**). For stoichiometric surfaces, the facets differ in the density of CUS sites (**Table S1**), as well as the extent of their coordination—only four-fold for (001) and mixed four-fold and five-fold for (111) but only five-fold for all other facets as shown in **Fig. 1A** (highlighted in yellow). We link these differences in geometry and coordination to a unique evolution of surface adsorbates under oxidizing conditions

and ultimately, OER activity. We measured the OER activity through cyclic voltammetry (CV) in **Fig. 1B** as well as chronoamperometry (CA) in **Fig. S2**. Normalizing current to oxide geometric surface area gives facet-dependent activity that spans more than an order of magnitude, which trend was preserved for OER activity per active site estimated from pseudo-capacitive charge[21] (**Fig. 1C**, **Table S2, Fig. S3**). In a previous study, we demonstrated that RuO_2 thin film exhibits approximately an order of magnitude higher OER current density compared to IrO_2.[15] Interestingly, here, we found that IrO_2 is significantly more influenced by film orientation compared to RuO_2 thin films.[16] For IrO_2, the activity of (100), (110), and (001) is significantly greater than the other facets of (101), and (111). These activities agree with those observed for ~7 nm particles that primarily have (110) and (101) facets.[2]

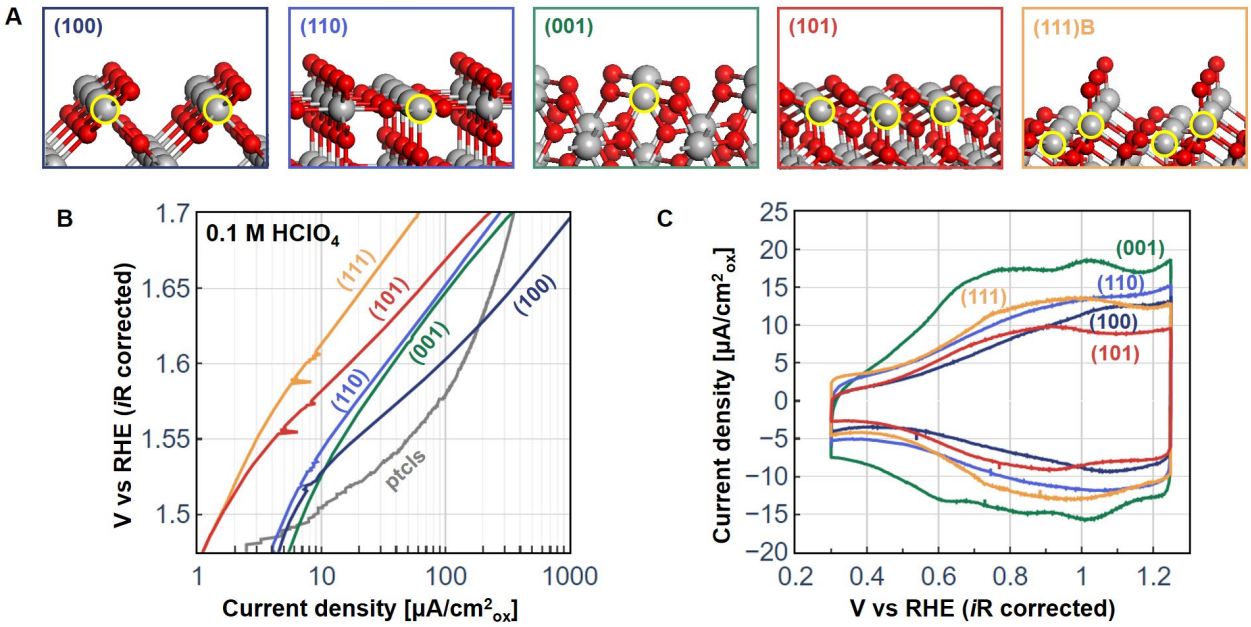

Fig. 1. (**A**) Surface geometries of five stoichiometric IrO_2 facets. The coordinatively unsaturated site (CUS) is highlighted as yellow circle. (**B**) Experimental OER activity for 5 facets, measured in O_2-saturated electrolyte in 0.1 M $HClO_4$. The forward and reverse sweep of the 2nd CV cycle were averaged to correct for capacitance. Similar trends were observed by chronoamperometry (CA) (**Fig. S2**). CV data for IrO_2 nanoparticles (ptcls) extracted from Lee et al. and normalized to

surface areas extracted from TEM.[2] (**C**) Redox features, measured in Ar-saturated electrolyte, below OER onset.

To understand the origin of OER activity, we examined facet-dependent Ir redox features in Ar-saturated 0.1 M $HClO_4$ at potentials below the onset of OER (**Fig. 1C**). These redox features have been referred to as specific redox couples, and redox features are dependent on facet,[22] indicating the binding of deprotonated adsorbates from H_2O such as *O and *OH on the active sites, which can be correlated with the catalytic activity.[23] We performed DFT calculations to predict the evolution of surface speciation as a function of applied potential on these five facets including two different terminations of (111) facet, (111)A and (111)B. The free energy was computed ranging from the fully reduced surface which is covered by water (μ_1-H_2O) and all bridge hydroxide (μ_2-OH), to the fully oxidized surface, where the surface consists of 1-fold terminal oxo (μ_1-O) and 2-fold bridge oxo (μ_2-O) species as shown in **Fig. S4**. In particular, on the (111)B facet, two distinct μ_1-O sites are identifiable. One is bonded to the low-coordinated surface site Ir_{4c}, while the other is associated with the high-coordinated surface site Ir_{5c}, both situated on the stoichiometric surface (**Fig. S4R**) which are referred to as μ_{1L}- and μ_{1H}- respectively. The adsorbate-adsorbate interaction is explicitly included for various configurations and all μ_1- species are bonded to the Ir CUS sites (yellow circle in Figure 1A) regardless of facet orientation.

Fig. 2A to **2E** show the evolution of equilibrium intermediate coverage with applied potential derived from the predicted surface free energy for the five facets (**Fig. S5A** to **S5F**). The gradient of the coverage for each species (**Fig. 2F** to **2J**) quantifies the contribution of a redox couple to a CV feature. The amount of charge density flowed from the redox reactions were calculated by summing up the number of redox reactions to reach the equilibrium state at a potential from the fully reduced state (**Fig. S5M** to **S5R**). Taking the gradient of the charge density with respect to potential multiplied by the scan rate of 50 mV/s gives CV's analogous to our experiment (**Fig. 2K** to **2O**).[24] A more detailed description is included in the **Supplementary Materials**. Remarkably, the general redox features agree well between theory and experiment, providing unprecedented atomistic insights into the evolution of surface adsorbates. The magnitude of computed current densities also agrees well with experiments, where experimental values are expected to be slightly higher from small amounts of roughness on the thin film surfaces (**Fig. S1 and Table S2**).

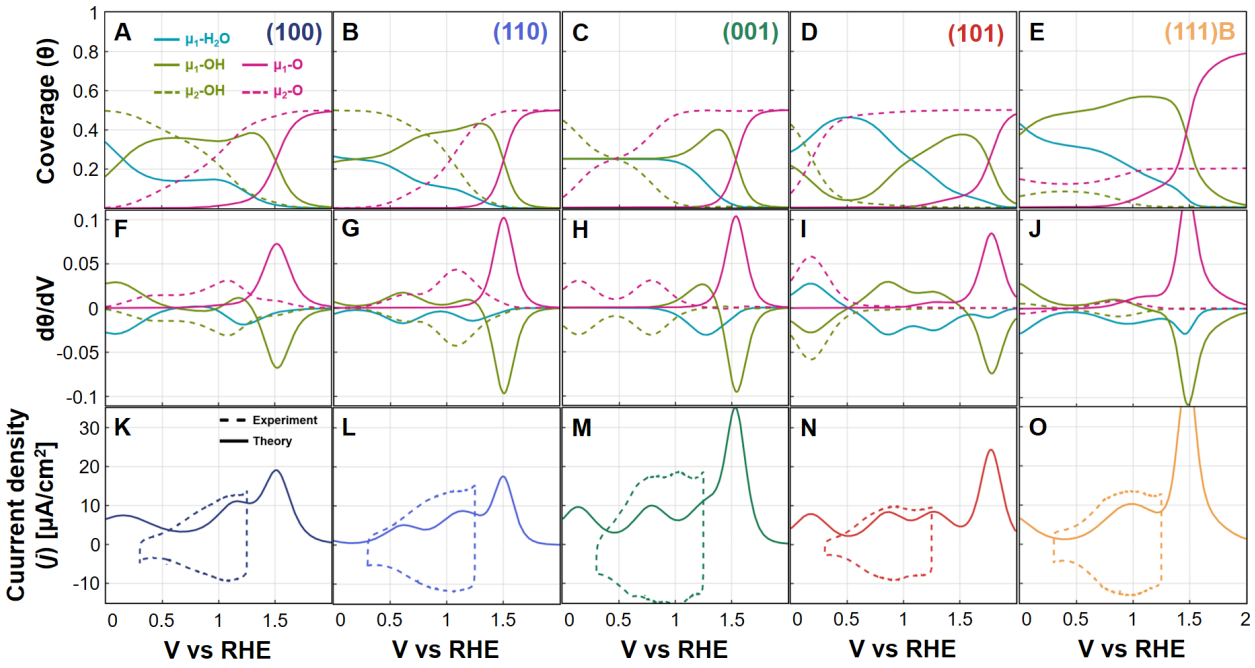

Fig. 2. Predicted surface intermediate coverages and experimental cyclic voltammetry (CV) curves (**A** to **E**) Evolution of equilibrium surface intermediate coverages as a function of applied potential for the five IrO_2 facets. The turquoise, light green, and pink lines represent the surface-bound H_2O, OH, and O, respectively. The solid lines indicate the 1-fold (μ_1-) and the dashed lines 2-fold (μ_2-) species. Summing all μ_1- and μ_2- species leads to unity. (**F** to **J**) The gradient of the surface intermediate coverages as a function of potential. (**K** to **O**) Comparison between the predicted current density from surface oxidation (solid line) and the experimental CV curve (dashed line).

We assigned these oxidation peaks to the following redox reactions. On (100) and (110), the major redox features near 1 V_{RHE} mostly originate from the μ_2-OH/μ_2-O redox pair, with a minor contribution of μ_1-H_2O/μ_1-OH couple. The gradient of different coverages (**Fig. 2F** to **2J**) allows the deconvolution of an apparent single redox peak into multiple redox reactions. For example, the 0.62 V_{RHE} peak on (110) has contributions from two redox pairs, μ_2-OH/μ_2-O and μ_1-H_2O/μ_1-OH with a ratio of 1 : 1.17.

For (001), all the redox features come from μ_2-OH/μ_2-O at potentials up to 1.03 V_{RHE} and then from μ_1-H_2O/μ_1-OH up to 1.34 V_{RHE}, where the latter appears as a shoulder peak, having its intrinsic maximum at 1.24 V_{RHE} which can be seen clearly in the gradient plot (**Fig. 2H**).

Interestingly, for (101), the peaks at both 0.86 V_{RHE} and 1.30 V_{RHE} originate mostly from the reduction of water to μ_2-OH. However, each corresponds to different configurations: 2μ_1-H_2O/(μ_1-OH+μ_1-H_2O) and (μ_1-OH+μ_1-H_2O)/2μ_1-OH (**Table S3**), respectively, which shows the importance of adsorbate-adsorbate interactions.

Among two (111) terminations, (111)B leads to closer agreement with experimental CV compared to (111)A (**Fig. S5W**) indicating that the (111)B is the dominant surface phase in our experiment. The peak at 0.99 V_{RHE} has three partial contributions, 47.5% from μ_1-OH/μ_1-O, 28.9 % from μ_2-OH/μ_2-O, and 23.7 % from μ_1-H_2O/μ_1-OH.

Overall, our predictions indicate that most of the experimental CV features between 0.30 and 1.23 V_{RHE} originate from μ_2-OH/μ_2-O for (100), (110), and (001) and μ_1-H_2O/μ_1-OH for (101) and (111)B. This difference originates from the high stability of μ_2-O on (101) and (111)B as the bond strength between Ir and μ_2-O correlates well with the onset potential for μ_2-OH/μ_2-O transition. (**Fig. S6**)

Interestingly, we found that the equilibrium μ_1-O density already captures the key trends of the facet-dependent OER activity suggesting μ_1-O is required as a precursor to O_2 evolution.[14,16] The highest peak for μ_1-O formation from **Fig. 2F to 2J** locates at 1.52 V_{RHE} for (100), 1.51 V_{RHE} for (110), 1.54 V_{RHE} for (001), 1.78 V_{RHE} for (101), and 1.48 V_{RHE} for (111)B leading to higher μ_1-O density at 1.6 V_{RHE} for highly active (100), (110), and (001) facets compared to less active (101) as shown in **Fig. S7**. However, (111)B stands out as a clear exception, suggesting that the reactivity of μ_1-O could be notably lower than that of other cases. Therefore, it is necessary to explicitly compute the OER energetics on each local atomic configuration of a facet in order to explain the OER trend.

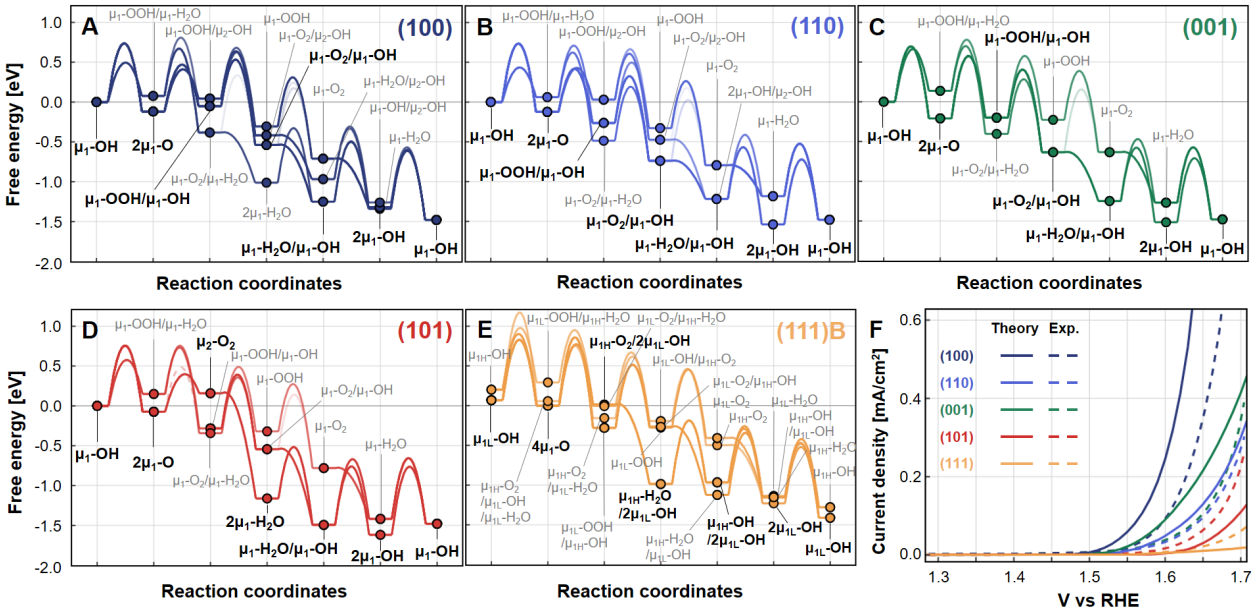

Fig. 3. Free energy landscape for the OER pathway at 1.60 V_{RHE} on (**A**) (100) facet, (**B**) (110) facet, (**C**) (001) facet, (**D**) (101) facet and (**E**) (111)B facet. The reaction coordinates of the most favorable pathway have bold black labels while those for minor pathways have thin grey labels. For clarity, labels of oxo species (μ_1-O, μ_2-O) are omitted. The opacity of lines represents the kinetics of each elementary reaction step in a logarithmic scale. (**F**) Comparison between theoretical (solid) and experimental (dashed) LSV curves for the five facets. For geometric representations of the most favorable pathway are shown in **Fig. 4**.

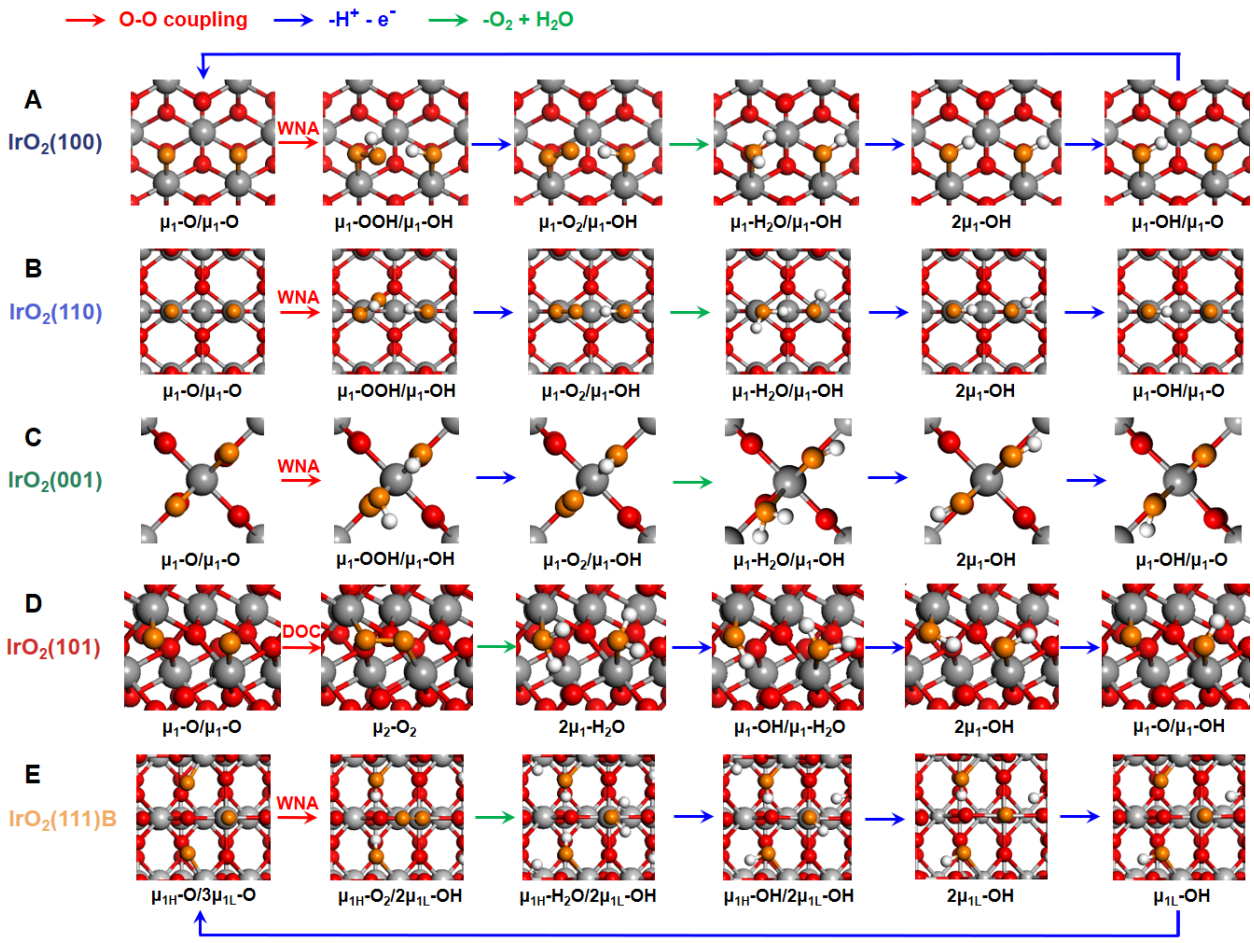

Fig. 4. The most favorable OER pathway for each of the five IrO_2 facets (**A**) (100) facet, (**B**) (110) facet, (**C**) (001) facet, (**D**) (101) facet, and (**E**) (111)B facet. The grey, red, and white spheres represent Ir, O, and H atoms, respectively, with orange representing adsorbed O. The red arrow denotes O-O coupling, the blue arrow denotes deprotonation, and the green arrow denotes O_2/H_2O exchange steps. On (100), (110), (001), and (111)B facets, the water nucleophilic attack (WNA) mechanism is favorable for O-O coupling while the direct oxo coupling (DOC) mechanism is dominant on the (101) facet.

To probe the origin of activity trends correctly, we examined the energetics of possible OER pathways for all facets considered. **Fig. 3A** to **3E** show the free energy landscapes of OER along the reaction coordinates for each facet at 1.60 V_{RHE} and the atomic configurations of elementary steps along the most favorable pathway are depicted in **Fig. 4**. To describe the reaction free energy

and the kinetic barrier of the potential-dependent non-electrochemical step, such as new O-O bond formation step, we employed the grand canonical potential kinetics (GCP-K) method[17] to obtain the reaction free energy and kinetic barrier as a function of applied potential (**Fig. S8**).

We considered three different pathways for the water nucleophilic attack (WNA) mechanism where water first attacks the electrophilic μ_1-O, leading to the new O-O bond by forming hydroperoxo (μ_1-OOH) while simultaneously transferring the other H to a nearby μ_1-O or μ_1-OH [5] or μ_2-O [7] site to form a μ_1-OH or μ_1-H_2O or μ_2-OH, respectively. The contribution of μ_2-O site to the total OER current density was found to be trivial at 1.60 V_{RHE} (**Fig. 3A to 3E** and Supporting Information Appendix). We also considered a direct oxo coupling (DOC) mechanism [25–27] for (101) and (001) (**Fig. S8**) based on the short distance between two μ_1-O (**Table S1**).

The energetics of the WNA mechanism is potential-dependent since an anodic potential makes μ_1-O more electrophilic, but the DOC mechanism shows a weak potential dependence (**Fig. S8**). The rest of the elementary steps along the OER pathway are also described grand canonically, but coupled to the Bell–Evans–Polanyi relationship[28,29] which assumes a linear dependence of kinetic barrier on reaction energy allowing efficient exploration of various oxidation steps on different surfaces. The whole reaction network was established by considering all possible connections between those states (**Fig. 3A** to **3E**). Then, the theoretical current density (**Fig. 3F**) was obtained using the microkinetic analysis with the steady-state assumption (see **Supplementary Materials** for further details). For each facet, the major OER pathway (**Fig. 4**) was determined by the fastest kinetics. The predicted OER current density (j) is in excellent agreement with the experiment (**Fig. 3F**), successfully following the trend of $j_{(100)} > j_{(001)} > j_{(110)} > j_{(101)} > j_{(111)B}$. Compared to the experimental results, the disparities in current density between facets were predicted to be more significant which may stem from the ideal flat facets in our theory which are different from those in experiments, potentially involving edges and other surface terminations.

Here we discuss mechanistic details responsible for the activity trend at 1.6 V_{RHE} for these facets. The (100), (110), and (001) facets —all highly active—share a similar main pathway through the μ_1-OOH/μ_1-OH state based on the WNA mechanism (**Fig. 4A** to **4C**), which have deprotonation steps through μ_1-O_2/μ_1-OH and 2μ_1-OH states. While the WNA occurs on two Ir sites for the (100) and (110) facets, it occurs through a chelating transition state (η^2-H_2O) on the (001) facet (**Fig.**

S9C), which has 0.11 eV lower barrier compared to the WNA involving two Ir (**Fig. S10**). The DOC mechanism is excluded due to the very high barrier (**Fig. S11**).

On (101) with two μ_1-O close to each other (2.77 Å, **Table S1**), the DOC mechanism has a lower kinetic barrier than WNA (**Fig. S8B**). After O-O coupling followed by O_2/H_2O exchange, the two intermediates take turns being oxidized toward the $2\mu_1$-O state (**Fig. 4D**).

On (111)B, WNA involves $2\mu_L$-O as proton acceptors leading to μ_{1H}-$O_2/2\mu_{1L}$-OH with a higher barrier compared to WNA on other facets (**Fig. 4E** and **S8B**). Following the O_2/H_2O exchange and the subsequent μ_{1H}-H_2O oxidation to μ_{1H}-OH, the μ_{1H}-OH undergo deprotonation to form μ_{1H}-O prior to $2\mu_{1L}$-OH species.

On (111)A, the proton is transferred to μ_2-O rather than μ_1-O during the WNA forming the μ_2-OH/μ_1-OOH state (**Fig. S12A** and **S12B**) because of the large distance between μ_1-O (5.52 Å). Due to intrinsically unstable μ_2-OH state at 1.6 V_{RHE} (**Fig. S5K**), this step is highly endothermic (+0.65 eV) with a high barrier of 0.81 eV (**Fig. S12A** to **S12C**) which leads to a notably small current density of < 0.2 nA/cm^2 at 1.6 V_{RHE}. This further verify that the (111)B is dominant in our experiments.

We further performed a sensitivity analysis to identify which elementary reaction step limits the overall current density for each facet. We employed the degree of rate control (DRC) method[30] to estimate the influence of each elementary reaction step on the net reaction rate, thereby identifying the rate-determining step (RDS). This analysis (**Fig. S13**) indicates that the O-O coupling step through WNA limits the OER current at > 1.6 V_{RHE} for (001) and (111)B while deprotonation is the RDS for (100), (110), and (101). This difference can be attributed to higher barrier of O-O coupling for (001) and (111)B (**Fig. S8B**), having 0.79 eV and 0.77 eV at 1.6 V_{RHE}, respectively, compared to 0.59 eV for (100), 0.54 eV for (110), and 0.46 eV for (101) along the most favorable OER pathway (**Fig. 4A** to **4E**). The WNA becomes rate-limiting at higher potential on (001) and (111)B facets due to a much weaker potential dependence of the barrier (-0.1 ~ -0.2 eV/V, **Fig. S8B**) compared to that of deprotonation barrier (~ -0.5 eV/V).

The (100) facet has the highest OER activity due to both a low O-O coupling barrier and to overall exothermicity of deprotonation steps at 1.6 V_{RHE}. Interestingly, we found the proton release from μ_1-OOH stabilized by an adjacent μ_1-OH through hydrogen bonding (1.721 Å , **Fig. S9F**) is rate-

limiting for (100) which was suggested in our previous work on RuO_2(110).[6] This oxidation reaction also becomes rate-limiting for (001) and (111)B facets at lower potential, and it makes a marginal contribution to the OER rate on (110).

Distinct from other facets, the overall kinetics on (110) and (101) facets is governed by μ_1-OH oxidation, owing to the less stable μ_1-O state. This RDS is related to the μ_1-OH/μ_1-O redox couple, which requires a higher potential on the (101) compared to the (110). Consequently, it elucidates the lower OER activity observed on the (101) facet. The crystal orbital Hamilton populations (COHP) analysis [31] indicates that the (110) and (101) surfaces exhibit the 2nd and 1st antibonding characteristics between surface Ir and μ_1-O, respectively (**Fig. S14**). We found a significant antibonding contribution of the t_{2g} band,[32] which explains the low stability of μ_1-O on these two facets. Additionally, μ_1-OH on the (101) facet is further stabilized by a highly-structured HB network with uniform 1.92 Å distance (**Fig. S15D**), leading to the highest overpotential to form an active μ_1-O species (**Table S3, Fig. S7**).

The involvement of PCET in the RDS for the most active (100) facet provides direction for efforts in improving IrO_2 OER activity. Firstly, catalyst design should target prevalence of the (100) facet while minimizing the presence of (101) and (111) facets using plane-selective capping or etching agent during the catalysts synthesis.[33] Secondly, approaches should be considered to modulate the interface environment in ways that facilitate the oxidation of intermediates by modulating such as pH, buffer or anion of electrolyte,[34–37] or analogous promotion of proton transfer at the catalyst-ionomer interface at the device level.

In summary, we observed that OER activity varies by an order of magnitude depending on the orientation of IrO_2 thin films despite the similar structural motif of octahedral IrO_6. We showed that various physical and chemical factors including atomic geometry, active site density, type of active sites, redox energetics, and OER pathways need to be combined into a single model to compare the direct voltammetry between theory and experiment to arrive at a comprehensive understanding of OER process at the atomic scale. Our approach facilitates assignment of redox peaks on the heterogeneous catalyst surface, allowing the contributions from multiple redox couples to a single redox peak to be quantified, often assigning a single redox couple to multiple redox peaks. The full kinetic analysis validates our experimentally measured intrinsic activity of these facets, which provides guidance for interpreting experiments. Mechanistic guidelines

originating from geometric effects presented in this study are expected to facilitate new heterogeneous catalyst designs.

Supporting information

Experimental and computational details, additional experimental results and DFT calculations, Supporting Figures (S1 to S21), Tables (S1 to S6), and Appendix for Microkinetic Equations (PDF)

Author contributions

S.K. and K.A.S. contributed equally to this work.

Notes

The authors declare that they have no competing interests.

Data Availability

The data underlying this study are available in the published article and its Supporting Information.

Acknowledgements

The computational work was supported by the Liquid Sunlight Alliance, which is supported by the US Department of Energy, Office of Science, Office of Basic Energy Sciences, Fuels from Sunlight Hub under award no. DE-SC0021266 (W.A.G.) and by an individual fellowship from the Resnick Sustainability Institute at Caltech (S.K.). We used the Extreme Science and Engineering Discovery Environment (XSEDE) for DFT calculations, which is supported by National Science Foundation grant no. ACI-1548562 (W.A.G.). K.A.S. acknowledges support from the National Science Foundation under Grant No. 2041153. We thank Dr. Liang Qiao for the assistance with thin film preparation.

References

(1) Bernt, M.; Hartig-Weiß, A.; Tovini, M. F.; El-Sayed, H. A.; Schramm, C.; Schröter, J.; Gebauer, C.; Gasteiger, H. A. Current Challenges in Catalyst Development for PEM Water

Electrolyzers. *Chemie Ingenieur Technik* **2020**, *92* (1–2), 31–39. https://doi.org/10.1002/cite.201900101.
(2) Lee, Y.; Suntivich, J.; May, K. J.; Perry, E. E.; Shao-Horn, Y. Synthesis and Activities of Rutile IrO2 and RuO2 Nanoparticles for Oxygen Evolution in Acid and Alkaline Solutions. *J. Phys. Chem. Lett.* **2012**, *3* (3), 399–404. https://doi.org/10.1021/jz2016507.
(3) Geiger, S.; Kasian, O.; Shrestha, B. R.; Mingers, A. M.; Mayrhofer, K. J. J.; Cherevko, S. Activity and Stability of Electrochemically and Thermally Treated Iridium for the Oxygen Evolution Reaction. *J. Electrochem. Soc.* **2016**, *163* (11), F3132. https://doi.org/10.1149/2.0181611jes.
(4) Zhang, K.; Liang, X.; Wang, L.; Sun, K.; Wang, Y.; Xie, Z.; Wu, Q.; Bai, X.; Hamdy, M. S.; Chen, H.; Zou, X. Status and Perspectives of Key Materials for PEM Electrolyzer. *Nano Research Energy* **2022**, *1* (3), e9120032. https://doi.org/10.26599/NRE.2022.9120032.
(5) Ping, Y.; Nielsen, R. J.; Goddard, W. A. I. The Reaction Mechanism with Free Energy Barriers at Constant Potentials for the Oxygen Evolution Reaction at the IrO2 (110) Surface. *J. Am. Chem. Soc.* **2017**, *139* (1), 149–155. https://doi.org/10.1021/jacs.6b07557.
(6) Rao, R. R.; Kolb, M. J.; Halck, N. B.; Pedersen, A. F.; Mehta, A.; You, H.; Stoerzinger, K. A.; Feng, Z.; Hansen, H. A.; Zhou, H.; Giordano, L.; Rossmeisl, J.; Vegge, T.; Chorkendorff, I.; Stephens, I. E. L.; Shao-Horn, Y. Towards Identifying the Active Sites on RuO2(110) in Catalyzing Oxygen Evolution. *Energy Environ. Sci.* **2017**, *10* (12), 2626–2637. https://doi.org/10.1039/C7EE02307C.
(7) Nong, H. N.; Falling, L. J.; Bergmann, A.; Klingenhof, M.; Tran, H. P.; Spöri, C.; Mom, R.; Timoshenko, J.; Zichittella, G.; Knop-Gericke, A.; Piccinin, S.; Pérez-Ramírez, J.; Cuenya, B. R.; Schlögl, R.; Strasser, P.; Teschner, D.; Jones, T. E. Key Role of Chemistry versus Bias in Electrocatalytic Oxygen Evolution. *Nature* **2020**, *587* (7834), 408–413. https://doi.org/10.1038/s41586-020-2908-2.
(8) Kuo, D.-Y.; Paik, H.; Kloppenburg, J.; Faeth, B.; Shen, K. M.; Schlom, D. G.; Hautier, G.; Suntivich, J. Measurements of Oxygen Electroadsorption Energies and Oxygen Evolution Reaction on RuO2(110): A Discussion of the Sabatier Principle and Its Role in Electrocatalysis. *J. Am. Chem. Soc.* **2018**, *140* (50), 17597–17605. https://doi.org/10.1021/jacs.8b09657.
(9) Opalka, D.; Scheurer, C.; Reuter, K. Ab Initio Thermodynamics Insight into the Structural Evolution of Working IrO2 Catalysts in Proton-Exchange Membrane Electrolyzers. *ACS Catal.* **2019**, *9* (6), 4944–4950. https://doi.org/10.1021/acscatal.9b00796.
(10) Dickens, C. F.; Kirk, C.; Nørskov, J. K. Insights into the Electrochemical Oxygen Evolution Reaction with Ab Initio Calculations and Microkinetic Modeling: Beyond the Limiting Potential Volcano. *J. Phys. Chem. C* **2019**, *123* (31), 18960–18977. https://doi.org/10.1021/acs.jpcc.9b03830.
(11) Exner, K. S.; Over, H. Beyond the Rate-Determining Step in the Oxygen Evolution Reaction over a Single-Crystalline IrO2(110) Model Electrode: Kinetic Scaling Relations. *ACS Catal.* **2019**, *9* (8), 6755–6765. https://doi.org/10.1021/acscatal.9b01564.
(12) Geppert, J.; Röse, P.; Czioska, S.; Escalera-López, D.; Boubnov, A.; Saraçi, E.; Cherevko, S.; Grunwaldt, J.-D.; Krewer, U. Microkinetic Analysis of the Oxygen Evolution Performance at Different Stages of Iridium Oxide Degradation. *J. Am. Chem. Soc.* **2022**, *144* (29), 13205–13217. https://doi.org/10.1021/jacs.2c03561.
(13) Rao, R. R.; Kolb, M. J.; Hwang, J.; Pedersen, A. F.; Mehta, A.; You, H.; Stoerzinger, K. A.; Feng, Z.; Zhou, H.; Bluhm, H.; Giordano, L.; Stephens, I. E. L.; Shao-Horn, Y. Surface

Orientation Dependent Water Dissociation on Rutile Ruthenium Dioxide. *J. Phys. Chem. C* **2018**, *122* (31), 17802–17811. https://doi.org/10.1021/acs.jpcc.8b04284.
(14) Rao, R. R.; Kolb, M. J.; Giordano, L.; Pedersen, A. F.; Katayama, Y.; Hwang, J.; Mehta, A.; You, H.; Lunger, J. R.; Zhou, H.; Halck, N. B.; Vegge, T.; Chorkendorff, I.; Stephens, I. E. L.; Shao-Horn, Y. Operando Identification of Site-Dependent Water Oxidation Activity on Ruthenium Dioxide Single-Crystal Surfaces. *Nat Catal* **2020**, *3* (6), 516–525. https://doi.org/10.1038/s41929-020-0457-6.
(15) Stoerzinger, K. A.; Qiao, L.; Biegalski, M. D.; Shao-Horn, Y. Orientation-Dependent Oxygen Evolution Activities of Rutile IrO2 and RuO2. *J. Phys. Chem. Lett.* **2014**, *5* (10), 1636–1641. https://doi.org/10.1021/jz500610u.
(16) Stoerzinger, K. A.; Diaz-Morales, O.; Kolb, M.; Rao, R. R.; Frydendal, R.; Qiao, L.; Wang, X. R.; Halck, N. B.; Rossmeisl, J.; Hansen, H. A.; Vegge, T.; Stephens, I. E. L.; Koper, M. T. M.; Shao-Horn, Y. Orientation-Dependent Oxygen Evolution on RuO2 without Lattice Exchange. *ACS Energy Lett.* **2017**, *2* (4), 876–881. https://doi.org/10.1021/acsenergylett.7b00135.
(17) Huang, Y.; Nielsen, R. J.; Goddard, W. A. I. Reaction Mechanism for the Hydrogen Evolution Reaction on the Basal Plane Sulfur Vacancy Site of MoS2 Using Grand Canonical Potential Kinetics. *J. Am. Chem. Soc.* **2018**, *140* (48), 16773–16782. https://doi.org/10.1021/jacs.8b10016.
(18) Liu, C.; Qian, J.; Ye, Y.; Zhou, H.; Sun, C.-J.; Sheehan, C.; Zhang, Z.; Wan, G.; Liu, Y.-S.; Guo, J.; Li, S.; Shin, H.; Hwang, S.; Gunnoe, T. B.; Goddard, W. A.; Zhang, S. Oxygen Evolution Reaction over Catalytic Single-Site Co in a Well-Defined Brookite TiO2 Nanorod Surface. *Nat Catal* **2021**, *4* (1), 36–45. https://doi.org/10.1038/s41929-020-00550-5.
(19) Sundararaman, R.; Goddard, W. A., III; Arias, T. A. Grand Canonical Electronic Density-Functional Theory: Algorithms and Applications to Electrochemistry. *The Journal of Chemical Physics* **2017**, *146* (11), 114104. https://doi.org/10.1063/1.4978411.
(20) Hörmann, N. G.; Andreussi, O.; Marzari, N. Grand Canonical Simulations of Electrochemical Interfaces in Implicit Solvation Models. *The Journal of Chemical Physics* **2019**, *150* (4), 041730. https://doi.org/10.1063/1.5054580.
(21) Burke, L. D.; Murphy, O. J. Cyclic Voltammetry as a Technique for Determining the Surface Area of RuO2 Electrodes. *Journal of Electroanalytical Chemistry and Interfacial Electrochemistry* **1979**, *96* (1), 19–27. https://doi.org/10.1016/S0022-0728(79)80299-5.
(22) Marković, N. M.; Grgur, B. N.; Ross, P. N. Temperature-Dependent Hydrogen Electrochemistry on Platinum Low-Index Single-Crystal Surfaces in Acid Solutions. *J. Phys. Chem. B* **1997**, *101* (27), 5405–5413. https://doi.org/10.1021/jp970930d.
(23) Man, I. C.; Su, H.-Y.; Calle-Vallejo, F.; Hansen, H. A.; Martínez, J. I.; Inoglu, N. G.; Kitchin, J.; Jaramillo, T. F.; Nørskov, J. K.; Rossmeisl, J. Universality in Oxygen Evolution Electrocatalysis on Oxide Surfaces. *ChemCatChem* **2011**, *3* (7), 1159–1165. https://doi.org/10.1002/cctc.201000397.
(24) Karlberg, G. S.; Jaramillo, T. F.; Skúlason, E.; Rossmeisl, J.; Bligaard, T.; Nørskov, J. K. Cyclic Voltammograms for H on Pt(111) and Pt(100) from First Principles. *Phys. Rev. Lett.* **2007**, *99* (12), 126101. https://doi.org/10.1103/PhysRevLett.99.126101.
(25) Wang, L.-P.; Van Voorhis, T. Direct-Coupling O2 Bond Forming a Pathway in Cobalt Oxide Water Oxidation Catalysts. *J. Phys. Chem. Lett.* **2011**, *2* (17), 2200–2204. https://doi.org/10.1021/jz201021n.

(26) Lin, C.; Li, J.-L.; Li, X.; Yang, S.; Luo, W.; Zhang, Y.; Kim, S.-H.; Kim, D.-H.; Shinde, S. S.; Li, Y.-F.; Liu, Z.-P.; Jiang, Z.; Lee, J.-H. In-Situ Reconstructed Ru Atom Array on α-MnO2 with Enhanced Performance for Acidic Water Oxidation. *Nat Catal* **2021**, *4* (12), 1012–1023. https://doi.org/10.1038/s41929-021-00703-0.
(27) González, D.; Heras-Domingo, J.; Sodupe, M.; Rodríguez-Santiago, L.; Solans-Monfort, X. Importance of the Oxyl Character on the IrO2 Surface Dependent Catalytic Activity for the Oxygen Evolution Reaction. *Journal of Catalysis* **2021**, *396*, 192–201. https://doi.org/10.1016/j.jcat.2021.02.026.
(28) Bell, R. P.; Hinshelwood, C. N. The Theory of Reactions Involving Proton Transfers. *Proceedings of the Royal Society of London. Series A - Mathematical and Physical Sciences* **1936**, *154* (882), 414–429. https://doi.org/10.1098/rspa.1936.0060.
(29) Evans, M. G.; Polanyi, M. Further Considerations on the Thermodynamics of Chemical Equilibria and Reaction Rates. *Trans. Faraday Soc.* **1936**, *32* (0), 1333–1360. https://doi.org/10.1039/TF9363201333.
(30) Campbell, C. T. The Degree of Rate Control: A Powerful Tool for Catalysis Research. *ACS Catal.* **2017**, *7* (4), 2770–2779. https://doi.org/10.1021/acscatal.7b00115.
(31) Dronskowski, R.; Bloechl, P. E. Crystal Orbital Hamilton Populations (COHP): Energy-Resolved Visualization of Chemical Bonding in Solids Based on Density-Functional Calculations. *J. Phys. Chem.* **1993**, *97* (33), 8617–8624. https://doi.org/10.1021/j100135a014.
(32) Ping, Y.; Galli, G.; Goddard, W. A. I. Electronic Structure of IrO2: The Role of the Metal d Orbitals. *J. Phys. Chem. C* **2015**, *119* (21), 11570–11577. https://doi.org/10.1021/acs.jpcc.5b00861.
(33) Wang, C.; Zhang, Q.; Yan, B.; You, B.; Zheng, J.; Feng, L.; Zhang, C.; Jiang, S.; Chen, W.; He, S. Facet Engineering of Advanced Electrocatalysts Toward Hydrogen/Oxygen Evolution Reactions. *Nano-Micro Lett.* **2023**, *15* (1), 52. https://doi.org/10.1007/s40820-023-01024-6.
(34) Fornaciari, J. C.; Weng, L.-C.; Alia, S. M.; Zhan, C.; Pham, T. A.; Bell, A. T.; Ogitsu, T.; Danilovic, N.; Weber, A. Z. Mechanistic Understanding of pH Effects on the Oxygen Evolution Reaction. *Electrochimica Acta* **2022**, *405*, 139810. https://doi.org/10.1016/j.electacta.2021.139810.
(35) Kamat, G. A.; Zamora Zeledón, J. A.; Gunasooriya, G. T. K. K.; Dull, S. M.; Perryman, J. T.; Nørskov, J. K.; Stevens, M. B.; Jaramillo, T. F. Acid Anion Electrolyte Effects on Platinum for Oxygen and Hydrogen Electrocatalysis. *Commun Chem* **2022**, *5* (1), 1–10. https://doi.org/10.1038/s42004-022-00635-1.
(36) Hausmann, J. N.; Menezes, P. W. Effect of Surface-Adsorbed and Intercalated (Oxy)Anions on the Oxygen Evolution Reaction. *Angewandte Chemie International Edition* **2022**, *61* (38), e202207279. https://doi.org/10.1002/anie.202207279.
(37) Bergmann, A.; Zaharieva, I.; Dau, H.; Strasser, P. Electrochemical Water Splitting by Layered and 3D Cross-Linked Manganese Oxides: Correlating Structural Motifs and Catalytic Activity. *Energy Environ. Sci.* **2013**, *6* (9), 2745–2755. https://doi.org/10.1039/C3EE41194J.

Abstract Graphics